

On the statistics of wind turbine wake meandering: An experimental investigation

Kevin B. Howard^{*}, Arvind Singh^{*}, Fotis Sotiropoulos^{*}, and Michele Guala^{*}

Citation: *Phys. Fluids* **27**, 075103 (2015); doi: 10.1063/1.4923334

View online: <http://dx.doi.org/10.1063/1.4923334>

View Table of Contents: <http://aip.scitation.org/toc/phf/27/7>

Published by the [American Institute of Physics](#)

On the statistics of wind turbine wake meandering: An experimental investigation

Kevin B. Howard,^{1,a)} Arvind Singh,^{1,2,b)} Fotis Sotiropoulos,^{1,c)}
and Michele Guala^{1,d)}

¹*St. Anthony Falls Laboratory and Department of Civil Environmental and Geo- Engineering,
University of Minnesota, Minneapolis, Minnesota 55414, USA*

²*Department of Civil, Environmental, and Construction Engineering, University of Central
Florida, Orlando, Florida 32816, USA*

(Received 16 December 2014; accepted 22 June 2015; published online 7 July 2015)

Measurements of the instantaneous wake flow from a model wind turbine placed in a turbulent boundary layer were obtained by wall-parallel oriented particle image velocimetry (PIV) in the St. Anthony Falls Laboratory wind tunnel. PIV velocity vector fields were used to investigate mean (expansion angle, wavelength, and wake velocity) and higher order statistics (local slope, curvature, and correlation) describing meandering motions in the turbine wake. These statistics were used to compare the wakes produced by four different wind turbine operating configurations, which include a single turbine operating at two different tip-speed ratios and two turbines aligned with the mean flow. The origin of meandering motions was identified for all cases in the hub vortex signature, which evolved into a stretched or compressed low speed meander in the wall parallel plane, depending on the turbine operating conditions and on the interaction with the wake shear layer. Finally, both autocorrelation and scale-dependent statistics on the velocity minima fluctuations about the meander signature suggest that small scale vortices, found in the hub shear layer and in the wake shear layer, interact with the hub vortex and govern its spatial evolution into large scale wake meandering. © 2015 AIP Publishing LLC. [<http://dx.doi.org/10.1063/1.4923334>]

I. INTRODUCTION

Meanders are primarily observed in erosional and depositional geophysical systems, such as rivers, tidal or submarine channels, and glaciers, where they are found to have different geometrical characteristics depending on local geomorphological processes, terrain and sediment characteristics, side and wall erosional rates, and vegetation cover among many other factors.^{1–8} Meandering flow patterns can however occur in other natural and anthropogenic systems, such as ocean streams, river mouth and planar jets,^{9–12} in the wakes of bridge piers, marine hydro-kinetic turbines, and wind turbines,^{13,14,16} and, at least qualitatively, share similar attributes with those observed in river networks and landscapes.

Among the different anthropogenic perturbations leading to meandering flows, we focus here on wind turbines and their wakes. Wake meandering has been addressed in detail in Ref. 17 and has also been found to originate from other rotating devices, such as hydro-kinetic turbines, designed to extract energy from river flows.^{16,18,19,34} Research in the area of renewable energy has been conducted in order to understand the complex flow produced in the wake of turbines, and subsequently, to formulate reduced complexity wake models, simulate large arrays at the power plant scale, and eventually optimize turbine siting under boundary conditions imposed by river bathymetry or

a)Electronic mail: howar539@umn.edu

b)Electronic mail: Arvind.Singh@ucf.edu

c)Electronic mail: fotis@umn.edu

d)Electronic mail: mguala@umn.edu

terrain topography. The main reason for increased research interest in wake prediction is that the preceding turbine's wake becomes the inflow for the next turbine and, consequently, controls its performance and operating condition, as well as its unsteady loads and structural health. First order turbine wake models (see Refs. 20 and 21 among many others) utilize a constant wake expansion angle along with a uniform velocity deficit which decreases at a defined rate, similar to a bluff body wake profile.²² The differences between hydro- and wind-turbines, however, include the Reynolds number of the incoming flow, specific blade and nacelle geometries, optimal tip-speed ratio (TSR), the relative position of the rotor within the boundary layer, terrain roughness, and complexity among many other factors. While these low order models are valuable to give initial estimates for either a hydro- or wind-turbine wake, models which consider the incoming turbulence provide the best results for evaluating flow statistics within turbine arrays²³ or wind turbine wake flows on complex terrain.²⁴ Further development upon these initial models,²⁵ with the inclusion of dynamic wake characteristics,²⁶ and atmospheric stability effects,²⁷ have shown that wake meandering characteristics need to be further investigated in terms of both additional large scale flow features in the wake and the influence of wake motion on downwind turbine performance and structural loading.²⁸ While several researchers investigated turbine wake motion,^{26,29–33} to the best of our knowledge, none has provided a detailed statistical description of wake meandering, as evolving from the hub vortices in the near wake. Farther from the rotor, large scale oscillations have been quantified by the Strouhal number $St = f_s D / U_{hub} \approx 0.1 - 0.2$, where D is the rotor diameter, U_{hub} is the mean incoming velocity at hub height, and f_s is the dominant frequency identified by the power spectrum of the streamwise velocity in the turbine wake.^{16,18} It remains thus to understand (i) how the hub vortex, which is shown to be inherently unstable,^{35,36} interacts with the tip vortex and rotor shear layer before wake meandering occurs and (ii) how the near and far wake can be re-defined based on the interaction between these dominant vortex structures. Here, we focus on wind turbine wakes immersed in the lowest $\sim 25\%$ of the turbulent boundary layer, as is the typical design configuration for utility-scale turbines in the atmospheric boundary layer.^{37,43} We employ miniature turbines in the St. Anthony Falls Laboratory (SAFL) wind tunnel using particle image velocimetry (PIV) flow measurements to investigate wake meandering characteristics for different turbine configurations in a spatial domain ranging approximately $0.5 - 4.1D$ in the streamwise direction and $-1D : 1D$ in the spanwise direction. In this study, we adopt a set of basic turbine arrangements to reproduce typical turbine operating conditions within a wind power plant array: first, single turbine at two different tip speed ratios, mimicking the adjusting of operating conditions and/or derating; second, two aligned turbines in the mean flow direction, representing turbines within a turbine array experiencing the effect of upwind turbine wakes. The major goal is to describe wake meandering statistically and quantify the changes undergone for the investigated turbine operating conditions or geometrical configurations. The experiments are designed to deploy the test turbine in a fully developed turbulent boundary layer flow, with mean shear across the turbine rotor consistent to values observed for utility-scale wind turbines. Measurements in the baseline confirmed that the turbine is exposed to the full spectrum of the incoming turbulent flow including the large and very-large scale motions described in Refs. 38 and 39, among others. The relevance of those structures is emphasized in the dynamic wake meandering (DWM) model by Ref. 26, according to which wake meandering oscillations can be passively driven by the incoming turbulence. In this experimental investigation, therefore, we have all the identified triggers of meandering motions, namely, wall turbulence and a miniature turbine model able to generate a hub vortex. This paper is outlined as follows. Section II provides a description of the wind tunnel, miniature wind turbine models, PIV setup and acquisition, and baseline flow, as well as a table listing the experiments conducted. Details on wake capture from the PIV and variable definitions and the results are presented and discussed in Section III. Discussion and Conclusions drawn from the research are provided in Secs. IV and V, respectively.

II. EXPERIMENTAL SETUP

Experiments were conducted in the closed circuit, atmospheric boundary layer wind tunnel at St. Anthony Falls Laboratory, University of Minnesota. The tunnel has a 200 horsepower fan

that blows down the 16 m long, 1.7 m by 1.7 m test section, with a 0.040 m tall picket fence trip placed after the 6.6:1 contraction to facilitate boundary layer growth and ensure realistic mean shear across the turbine rotor. The boundary layer was developed over smooth aluminum floor panels that can be temperature controlled independently from the free stream air in order to simulate various atmospheric thermal conditions. Herein, the floor and air temperatures were held equal at 24 °C to provide thermally neutral conditions. The ceiling panels in the test section were adjusted to maintain a nearly zero pressure gradient growth of the boundary layer. The wind turbine model used herein consisted of a fixed pitch, three-blade (GWS/EP-5030x3) rotor with a diameter $D = 0.128$ m. Similar turbine models have been used by Chamorro and Porté-Age,⁴⁰ Cal *et al.*,³⁷ España,⁴¹ and Hu *et al.*⁴² among others. Our rotor, placed with the blade high pressure surfaces facing the inflow, was directly connected to a DC generator fixed at a hub height of 0.104 m, which is able to produce a differential voltage signal proportional to the rotor angular velocity.⁴³ The generator has been characterized to have a linear increase in output with velocity, a characteristic of the motor design and internal friction,⁴³ and therefore maintains a nearly constant TSR of ≈ 5.2 in the free-spinning condition (i.e., when no outside voltage is applied to the generator). To adjust the TSR, and subsequently the power coefficient, an outside voltage is applied to the generator opposing the turbine rotation direction. The second TSR of 3.2 was selected, based on the miniature turbine performance curve, to provide the optimal power coefficient ($C_p \approx 0.27$). Note that the nacelle to rotor diameter ratio in our turbine model is approximately 0.09, which is larger than that of a utility-scale wind turbine (0.05 for the 2.5 MW Eolos turbine¹⁵) but smaller as compared to the hydrokinetic in-stream turbine.¹⁶ A TSI PIV system consisting of two 4 megapixel PowerView cameras, Insight 4G software, synchronizer, and a Big Sky 532 nm Nd:Yag laser was situated in a wall-parallel orientation such that it allowed the capture of streamwise and spanwise velocity fluctuations on a plane at hub height. Stitching the images from the two cameras together provided a field of view (FOV) of roughly $3.6D$ (≈ 0.46 m) in the streamwise direction and $1.8D$ (0.23 m) in the spanwise direction. This setup was used to capture the spanwise meandering and fluctuations in the wind turbine wake at hub height, where the rotation about the x -axis is assumed to be symmetric. The full FOV and camera arrangement are shown in Figure 1(a) with respect to the upwind and downwind turbines. The sampling rate for each case was 7.25 Hz, which is not fast enough to have time resolved movement of the wind turbine wake, but still provides data for ensemble averaging as well as spatially resolved instantaneous flow fields for the estimate of wake meandering statistics. The number of image pairs used herein was 700 for all of the cases except for the single turbine free-spinning test, where 1000 images were captured. The PIV could not be used to calculate the boundary layer statistics, due to the horizontal orientation; therefore, a vertical profile was taken with a two component hotwire anemometer. The hotwire was calibrated at the same 24 °C at ten angles between $\pm 30^\circ$ for nine velocities. The Dantec hotwire probe was

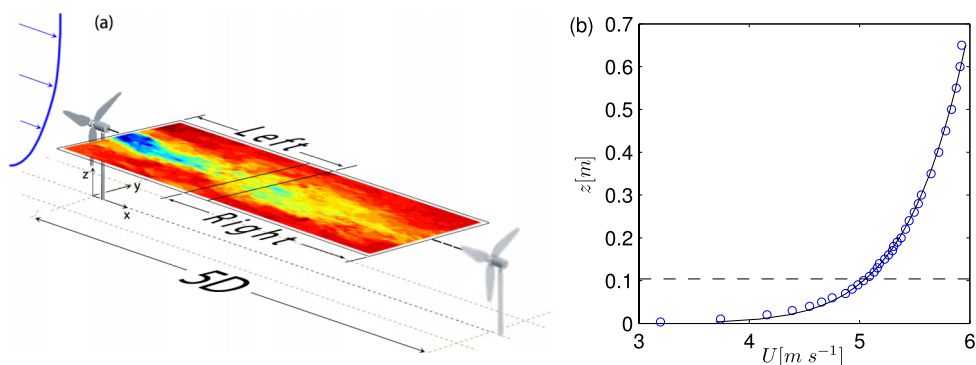


FIG. 1. (a) Schematic of the PIV sampling area in proximity to the turbines. The combined left and right cameras are capturing a wall-parallel field of view at hub height with a total streamwise length of just under $3.6D$ (≈ 0.46 m) and spanwise breadth of $1.8 D$ (0.23 m). (b) Boundary layer mean velocity profile as measured by the two component, hot-wire anemometer. The horizontal dashed line denotes the elevation where the wall-parallel PIV was captured (turbine hub height) and the solid black curve is a power law with an exponent of 0.09, for $U(z) = U_{hub}(z/z_{hub})^{1/0.09}$.

TABLE I. Flow statistics for turbulent boundary layer with $U_{hub} \approx 5 \text{ m s}^{-1}$ as measured by a hot-wire anemometer.

δ (m)	u_τ (m s ⁻¹)	U_{hub} (m s ⁻¹)	U_δ (m s ⁻¹)	Re_τ	Re_D	Re_δ
0.6	0.23	5.0	5.91	9200	42 977	236 440

connected to an A.A. Lab System amplifier and boundary layer data were acquired with LabVIEW at 10 000 Hz for 120 s at each elevation in the profile. More details on the hotwire setup and data acquisition can be seen in Howard *et al.*⁴³ and Singh *et al.*⁴⁴ The resulting boundary layer profile is presented in Figure 1(b), and also noted on the profile is the elevation of the PIV plane. All runs were conducted at $U_{hub} \sim 5 \text{ m s}^{-1}$ under neutral thermal conditions. The corresponding Reynolds numbers Re_τ , Re_D , and Re_δ were ~ 9200 , 42 977, and 236 440, respectively, where $Re_\tau = u_\tau \times \delta / \nu$, $Re_D = U_{hub} \times D / \nu$, and $Re_\delta = U_\delta \times \delta / \nu$; $u_\tau = 0.23 \text{ m s}^{-1}$ is the shear velocity, $\delta = 0.6 \text{ m}$ is the boundary layer thickness, and $\nu = 1.5 \times 10^{-5} \text{ m}^2 \text{ s}^{-1}$ is the kinematic viscosity of air, see Table I for all flow related details. Boundary layer statistics for the baseline case are presented in Figure 2, comprising mean and r.m.s streamwise velocity profile and power spectrum at hub height; note that the value of the smooth wall constant $B = 3.0$ reflects the limited roughness effects induced by the junctions between the aluminum panels of the wind tunnel wall.

Four different turbine configurations were tested in this study. The first is the single turbine operating as a derated turbine (no externally applied load, with only frictional torque), denoted hereafter as ST Free. The second test condition used a voltage applied to the turbine such that the turbine is operating at its optimal TSR, hereafter called Single Turbine-Optimal (ST Opt). The comparison of these first two tests not only provides an inspection of TSR effect on wake meandering but also coupled with that, the influence of the velocity deficit on wake characteristics. The last two experiments were designed to provide additional data on wake development in a turbine array by aligning two turbines in the streamwise direction with $5D$ spacing (spacing selected as it is a nominal distance used in wind farms today); PIV measurements captured the wake of the first turbine (Turbine-Turbine (TT)) and the wake of the second turbine (turbine-turbine wake (TT wake)). Details on these cases can be found in Table II.

III. RESULTS AND DISCUSSION

A. Wake capture and definitions

The instantaneous signature of meandering flow is defined, in each PIV realization, by the envelope of the minima of the streamwise velocity $u(x, y)$ in the turbine wake. The full PIV spatial resolution is used here to locate the velocity minimum in the y -direction (y range of $\pm 0.75D$), for each

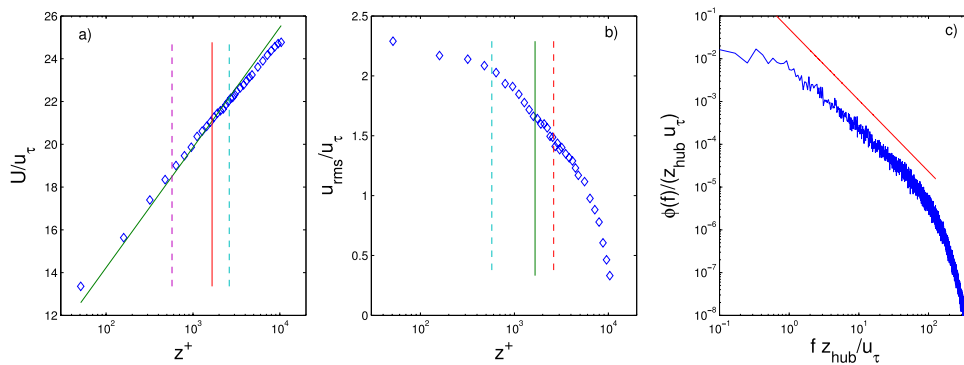


FIG. 2. Baseline flow conditions and boundary layer statistics: (a) mean velocity profile U/u_τ as a function of $z^+ = zu_\tau/\nu$, as compared to the logarithmic velocity profile $(1/k \log(z^+) + B)$ with $B = 3$ and $k = 0.41$ (vertical dashed and solid lines represent the bottom, top tip locations, and hub height, respectively); (b) streamwise r.m.s. velocity profile u_{rms}/u_τ ; (c) normalized streamwise velocity spectrum at hub height $\phi(f)$ with solid line providing $-5/3$ slope for reference.

TABLE II. Wind turbine configurations and operating conditions tested in the wind tunnel. In the turbine-turbine runs, the two units are aligned in the streamwise direction at a spacing of $5D$ measured from upwind rotor plane to downwind rotor plane. TSR denotes the tip-speed ratio and FOV is the PIV field of view in the x -direction in reference to the rotor plane of the upwind turbine, or first turbine in the case of two aligned turbines.

	Single turbine-free (ST Free)	Single turbine-optimal (ST Opt)	Turbine-turbine (TT)	Turbine-turbine wake (TT Wake)
TSR	5.2	3.2	5.2	5.2
FOV [x/D]	0.5–4.1	0.5–4.1	0.5–4.1	5.5–9.1

x -location, as shown in Figure 3. The resulting meander, different in each instantaneous flow field, starts just downwind of the hub and wanders, along with some smaller scale fluctuations, about a general oscillating trend. We acknowledge that the wake of the wind turbine is highly three-dimensional and rotates opposite to the rotor rotation direction;³¹ therefore, we are actually capturing a slice of the helicoidal wake motions.^{18,34} Despite this rotational component, the wall-parallel PIV plane can still describe the spanwise fluctuations of the turbine wake and, if coupled with wall-normal measurements, could help define the three-dimensional oscillations of the wake.

By observing the instantaneous, raw, unfiltered, meander signature ($u(x, y)$ minima marked as dots in Fig. 3), we recognize the oscillatory nature of a turbine wake and harken back to the smooth and gradual flow meandering. In order to follow the estimation of the mean meander quantities as introduced by the geomorphology community, the raw signal is low-pass filtered to produce a smooth, meandering signature, as shown by the white curve in Figure 3. Here, the cutoff wave number of the Fourier filter was set to allow spatial fluctuations scaling with the turbine rotor to persist in the low speed meander while removing the small scale content. In particular, the choice of the cutoff wavenumber in the Fourier based filter was dictated by two constraining factors: (1) the size of the field of view ~ 0.45 m, defining our largest measurable scale; (2) the turbine frequency ~ 54 Hz, corresponding to a time interval of 0.018 s, which, when projected in space using the mean wake velocity, defines a length scale of 0.065 m $\sim 0.5D$. In the effort to single out the large scale contributions of the low speed meander, within a continuum of energetic scales, we set the cutoff wavenumber as $k_{cut} \simeq 15.4 \text{ m}^{-1}$ ($k_{cut}D \simeq 2$) corresponding to a resolved length scale $L_{cut} = k_{cut}^{-1} \simeq 0.065 \text{ m} \simeq 0.50D$. The above estimated k_{cut} , specifically related to the derated single turbine case, was not changed in the other configurations to preserve the ability to compare between the cases. As a consequence of this choice, the smallest wavelength of the meander is set to $0.5D$. Smaller scales are attributed to the local effect of vortices around the meander shear layer, the rotor shear layer, and in general in the velocity deficit region. Effects of smaller scales on meander statistics will be addressed in Secs. III B–III F.

In Figure 4, a set of instantaneous vector fields are provided to demonstrate how the meandering flow large scale signature is modulated by small scale vortices generated in the turbine near wake. This figure displays four locations within the wake focused on the local flow minima. In

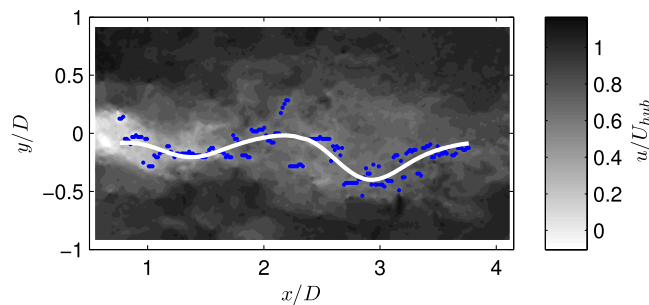


FIG. 3. Instantaneous velocity field contour from PIV in the wake of the single turbine free case: blue dots mark the x, y locations of the minimum streamwise velocity; the white curve represents the low-pass filtered meander signature. The filtered wake provides the basis for estimating the meander wavelength, which for this PIV instance would be $\lambda/D \approx 1.5$ as calculated from the local minima at $x/D \approx 3$ and 1.5.

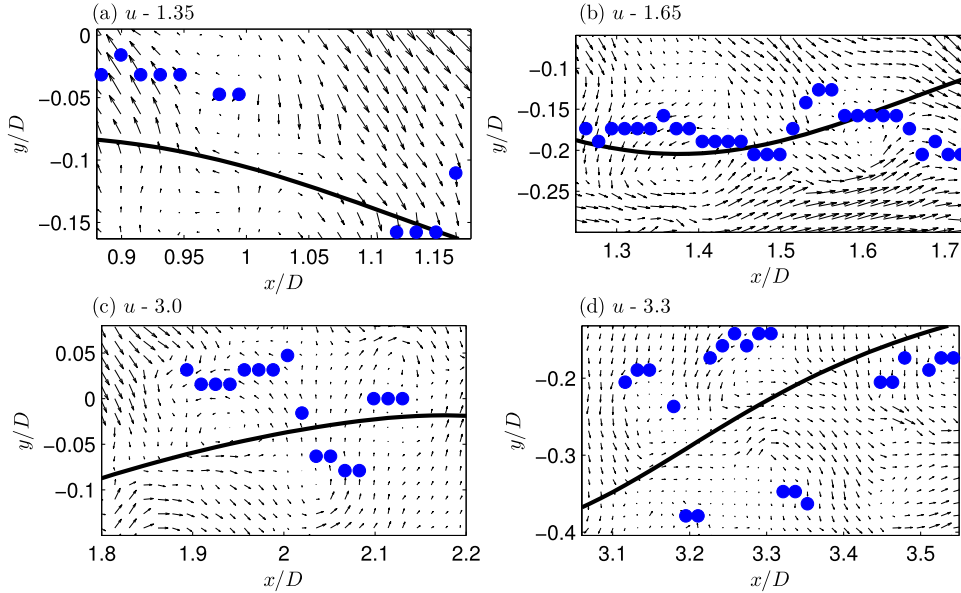


FIG. 4. Snapshots of u, v vector fields around selected, local streamwise velocity minima (blue dots) in relation to the spatially filtered wake signal (solid black curve). Instantaneous velocity fields are displayed after the subtraction of a constant streamwise wake velocity U_C in the following x -range: (a) $0.9 < x/D < 1.2$ with $U_C = 1.35 \text{ m s}^{-1}$, (b) $1.25 < x/D < 1.75$ with $U_C = 1.65 \text{ m s}^{-1}$, (c) $1.8 < x/D < 2.2$ with $U_C = 3.0 \text{ m s}^{-1}$, and (d) $3.05 < x/D < 3.55$ with $U_C = 3.3 \text{ m s}^{-1}$.

each of the panels in Figure 4, a constant streamwise (convection) velocity is removed from the instantaneous vector field to allow the exposure of vortices within the wake⁴⁵; each window shows that the wake minima primarily occur at the edges of vortices located close to the large scale flow meander (the solid curve). The various sources of vorticity are the turbine nacelle (generating the hub vortex), the blade tips, and the shear layers around both the hub and the rotor, in addition to potential interactions between the above structures. As evidenced in Figure 4, the velocity minima method cannot distinguish between the large scale wake meandering and the small scale vorticity; for this reason, a spatial low-pass Fourier filter on the raw $u(x, y)$ minima was implemented (to provide data with scale separation). Each instantaneous PIV vector field is analyzed in the same way to produce both the low-pass filtered wake as well as the fluctuations about the filtered wake. $l_{raw}(x)$ is defined as the location of the $u(x, y)$ minima (in the y -direction, for each x location) and $l_f(x)$ as the spatially smoothed curve defining the filtered flow meander. The signal for the spanwise small scale fluctuation of the wake is then computed by $l' = l_{raw} - l_f$. The result of this processing provides, for each turbine configuration, a number of instantaneous wake meanders $l_f(x)$ and corresponding fluctuations $l'(x)$ equal to the number of PIV vector fields. We stress that the high spatial resolution measurements provided in Figure 4 confirm that the fluctuations l' of the wake minima are physical, not a source of erroneous vectors from PIV interrogation, and therefore deserve further investigation to understand if, and how strongly, these small scale vortices interact with the larger scale meandering motion.

Next, we define the mean wake edge by marking the occurrence of the wake minima for all vector fields (the dots in Fig. 3) and defining a continuous, spatial x, y domain where instantaneous wake meanders traveled at least one time. The specific $y(x)$ position of the mean wake edge is then selected as the point, at each x location, delimiting an uninterrupted domain in the spanwise direction. This results in two fairly symmetrical curves, one at each side of the nacelle marking the left and right edges of the meander domain along the wind direction. It is important to recall that the wake domain is chosen to be spatially continuous, implying that no gaps exist in the y -distribution of wake minima occurrence; Figure 5(a) shows how the edges are defined for each x -location, distinguishing between the continuous meandering flow domain in the spanwise direction and the occurrence of rare velocity minima outside of such domain. These outer minima take place on average 0.3% of the time up to $x/D = 2$ and only increase to an occurrence of 1% at approximately

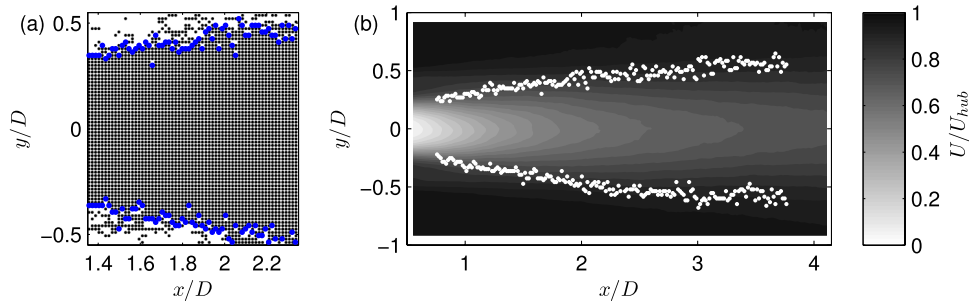


FIG. 5. (a) Local sample of the wake minima (black dots) representing the unconditioned wake domain (the continuous portion is delimited by the blue dots, defining the wake edges). (b) Full-scale distribution of the estimated wake edges (white dots) superimposed on the mean streamwise velocity contour as captured by wall-parallel PIV.

$x/D = 4$; they are thus regarded as extreme wake oscillation events and are not included in the mean wake edge definition. Statistically, the edge points correspond to the first and last empty bins of the spanwise distribution of wake minima. The resulting left ($+y$) and right ($-y$) edges identified for the single turbine case are shown in Figure 5(b) as white dots plotted on top of the mean streamwise velocity contour. The mean expansion angle is then computed as the angle between the x -axis and a linear fit through the points defining the edge.

B. Mean wake statistics

Before investigating the comparison between the four cases, we highlight a couple of interesting features observed in Fig. 5(b): first, the core of the mean velocity deficit region at the beginning of the wake edge, close the rotor plane, is fairly well confined in the spanwise direction, likely extending up to the shear layer introduced by the root and hub vortices; second, for $x/D > 2$, the wake edge experiences a higher variability in y position, as measured by the spanwise variance; it is hypothesized that this is due to the reduced strength of the wake edge shear layer with increased x/D position, especially after the hub shear layer interacts with the tip vortex shear layer. We also note that the meandering domain is expanding in the x direction at a highest rate with respect to the mean velocity in the wake, visibly crossing the iso-velocity contours up to $x/D \sim 2$. At that specific location, the edge of the meandering domain intersects also the blade tips, $y/D = \pm 0.5$, where the tip vortex is expected to show up in the horizontal PIV plane. This implies that at $x/D \sim 2$, the interaction between the tip and the hub vortex is possible, and thus that the flow meander may start to feel structures scaling with the rotor diameter, and not with the nacelle diameter. This is consistent with the evolution of the wake characteristics and mechanisms presented by Kang *et al.*³⁴ We stress again that turbine wake flow is highly three-dimensional, with a non-zero mean streamwise vorticity induced by the rotor angular velocity, which in fact results in a slightly asymmetric wake. The largest wake edge variation occurs near $x/D \sim 2$ on the left side (upper region in Figure 5(b)), which is inferred to be induced by the wake flow interacting with higher momentum fluid (creating a means of momentum transfer) caused by the wake counter-rotation. This increased variance only arises after the wake edge is out of the sheltering effect of the velocity deficit region produced by the rotor ($x/D > 2$). We infer that the instantaneous fluctuations of the wake edges and the spatial evolution of the near-wake meandering motions are governed by the interaction between the hub vortex and the higher momentum fluid entrained along the tip vortex shear layer, occurring at $x/D \approx 2$ for the data presented in Fig. 5(b). Some phenomenological aspects of this interaction, studied for hydro-kinetic turbines in Ref. 34, are addressed in Secs. III C–III F to improve our current definition of near and far turbine wakes.

C. Flow meandering statistics depending on turbine operational regime and siting configuration

The flow meander signature smoothly evolves from the turbine hub, under the local constraining effects exerted by the hub and root shear layers and corresponding vortices (near wake), and

by the tip vortex shear layer (far wake). As discussed above, there are qualitative and quantitative tools to distinguish between the near wake and the far wake, but a clear, unambiguous definition as a function of only the rotor diameters may not be possible due to (i) the influence of the specific nacelle and blade geometry and (ii) the transition region where both the hub vortex and the tip vortex interact and govern the observed flow meandering pattern (depending, e.g., on tip speed ratio, or inflow conditions). Therefore, to assess the specific influence of the turbine operating conditions on the wake flow, we consider here spatially averaged flow meandering statistics with no distinction between near and far wakes.

The comparison between the mean edge expansion angle γ for the four different cases is presented in Figure 6(a). It can be seen that for all of the turbine configurations, the left and right edge expansion angles are different. We hypothesize that the asymmetric expansion angle is caused by the primary rotation direction of the wake about the x -axis, shown in Ref. 31, induced by the equal and opposite reaction to the flow impacting the rotor. To ensure that this feature was not due to the streamwise velocity inhomogeneity in the spanwise axis of the tunnel, wall-parallel PIV measurements were conducted in the baseline flow as well, confirming variations of $U(y)$ smaller than 0.9% of the hub velocity, across the sampling region. Moreover, when comparing the two single turbine operating conditions, we found that the difference between the left and right edge angles is maximized for the ST Opt case where the turbine has a reduced TSR, as compared to ST Free. In the ST Opt case, the turbine is operating at peak efficiency, which means that the torque on the blades is increased, and subsequently, the counter-rotation of the wake is expected to be larger with respect to the ST Free case (higher TSR, but minimal torque). It is proposed that the inherent asymmetry of the turbine wake is amplified by the increased strength of the counter-rotation, causing the greater discrepancy between the two wake edges. The turbine rotor used in this set of experiments rotated in the counter-clockwise direction, when viewed from upwind; therefore, the wake flow is expected to rotate in a clockwise manner such that, at the left edge of the wake ($+y$), the primary out-of-plane velocity direction is in the $+z$ (out of the PIV domain) and oppositely for the right edge. The wake flow along the right edge then serves to transfer high momentum fluid down towards the wall. The second noteworthy trend in Figure 6(a) is the difference in mean expansion angle between the different cases studied here. The single turbine ST Free and the upwind turbine wake in the TT configuration exhibit relatively higher mean angles, as compared to the single turbine at optimal TSR (ST Opt) and the downwind TT wake. The similar behavior of the ST Free and TT (front turbine wake) is expected because both rotors (i) are exposed to the same incoming flow, (ii) have the same TSR, and thus (iii) induce the same velocity deficit. The trend between the four cases is confirmed through inspection of the amplitude of filtered wake signal, shown in Figure 6(b). However, the difference between ST Opt and ST Free is more subtle: a turbine operating at peak performance induces a larger velocity deficit and thus has a larger mean shear (at the wake edge) able to sustain the tip vortices along the x -axis. A strong tip vortex structure, harbored in the shear layer produced between the high momentum fluid outside the wake and a large velocity deficit, keeps the wake confined and limits the entrainment of high momentum fluid, resulting in

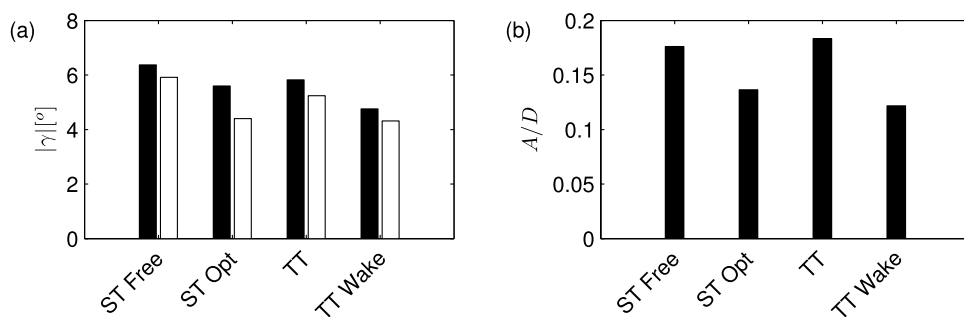


FIG. 6. (a) Comparison of edge expansion angle γ between multiple turbine configurations. The expansion angles calculated with the right edges ($-y$) are the black bars and the left edge ($+y$) angles are shown in white bars. (b) Amplitude of meander, computed as an average from local maximum to local minimum.

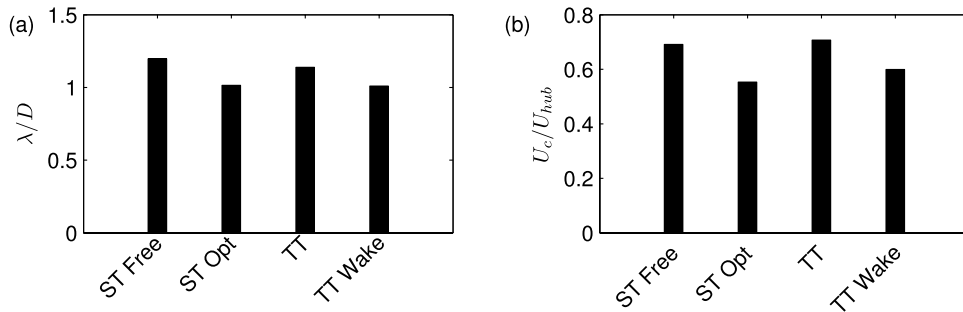


FIG. 7. (a) Comparison of wavelengths between the different experiments investigated herein. (b) Convection velocity U_c comparison in the wake of the different cases. U_{hub} for all cases is the hub velocity in the undisturbed boundary layer.

a smaller expansion angle. It is also argued that the expansion angle for the less efficient turbine cases must be a function of the pressure downwind of the rotor; however, as no direct pressure measurements were taken, we focused on the filtered wake meandering data and their interaction with the surrounding flow to gain a better perspective. Howard and Hemberger² suggested a range of approximately 50–60 meanders (a meander is classified as one wavelength) for good statistical convergence, implying that our number of captures per turbine configuration of >700 is well beyond the suggested length on an ensemble basis.

A comparison of the mean wavelength from the filtered wake signals for the different turbine configurations is shown in Figure 7(a). The wavelength is estimated as the length scale comprised between two consecutive local minima or local maxima of the low-pass filtered meandering signature: for instance, if we consider the meander in Figure 3, the local minima are precisely located at $x/D \approx 1.5$ and $x/D \approx 3$; therefore, we estimate $\lambda = 1.5D$, and so on for each realization. The overall change of the mean wavelength, between the various cases, follows the same trend presented by the edge expansion angle: larger expansion angle implies weaker wake shear layer, a lower velocity deficit (higher mean wake velocity) and a stretched meandering signature in the x -direction (thus, a larger λ). Accordingly, when the wake is produced by an efficient turbine, more streamwise momentum is extracted by the device, resulting in a larger velocity deficit in the wake (lower wake velocity) and a wake meander which has a lower wavelength. In the case of the aligned downwind turbine (TT wake), we infer that the deflection of large turbulent structures by the upwind turbine⁴³ to the wake edges is keeping the downwind turbine wake more confined; as a result, the velocity deficit is further increased, with respect to the front turbine hub velocity, resulting in increased wake shear and lower wake velocity (hence, low γ , low λ). The mean velocity in the wake U_c appears thus to be the key governing parameter for meandering that we can extract from PIV measurements. U_c is calculated using an area defined by the wake edge for each of the instantaneous PIV fields. As shown in Figure 7(b), the wake velocity for the cases with longer wavelengths (and greater wake expansion angle) is higher, as anticipated, as a higher wake velocity stretches the hub and tip vortex structures in the streamwise direction (measured by the increase in wavelength) but reduces the shear layer intensity at the wake edges. One important variable controlling at least phenomenologically, the above mean wake meandering statistics (γ , λ) appear therefore to be the wake velocity, or in another words, the velocity deficit. A larger velocity deficit compresses the wake meanders in both horizontal directions, while a lower velocity deficit induces the opposite effect. Obviously, specific velocity deficit results from specific turbine operating conditions.

D. A preliminary distinction between near and far wake meandering oscillations

Even though the explored field is limited to 4D in the streamwise direction, we observed a marked variability in the amplitude and wavelength of the flow meander. In particular, by plotting on the $\lambda/D, A/D$ phase space all the instantaneous low pass filtered meander characteristics, obtained for each PIV vector field, we recognize two different populations (see Figure 8). This is consistent with (1) the near wake signature of the hub vortex, as a distinct feature from the

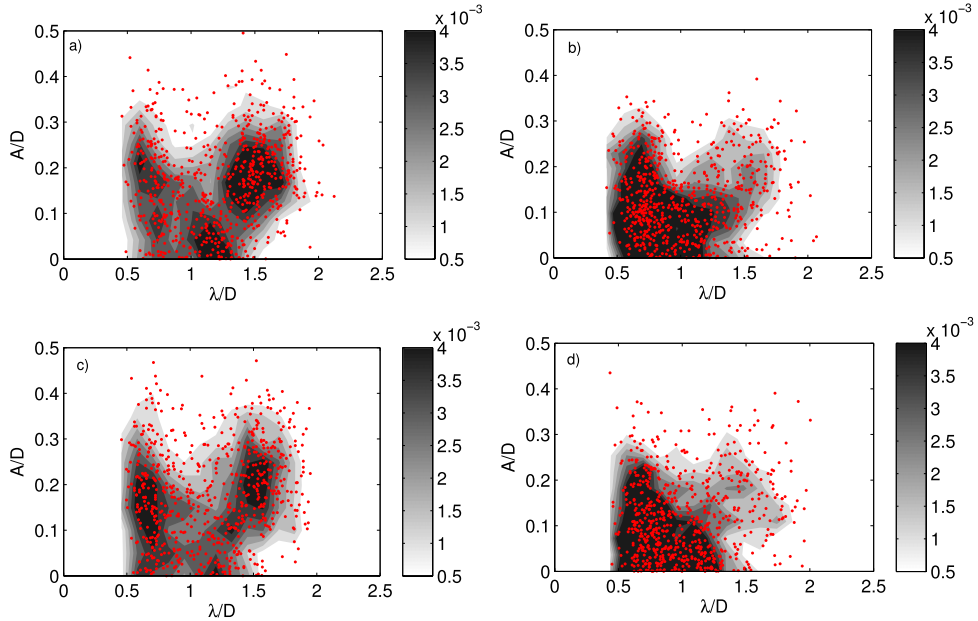


FIG. 8. Joint distribution of the meander amplitude and wavelength for the (a) single turbine free, (b) single turbine optimal, (c) turbine-turbine, and (d) turbine-turbine wake.

(2) far wake meandering. In terms of the Strouhal number, we can estimate the shedding frequency as the ratio between the wake velocity U_c and the estimated wavelength λ , leading to $St = f_s D / U_{hub} \simeq (U_c / \lambda) D / U_{hub} = \frac{U_c / U_{hub}}{\lambda / D}$. For the optimal tip speed ratio case, which has been extensively investigated in the literature, large scale oscillations lead to $St_{2opt} \simeq \frac{U_c / U_{hub}}{\lambda_2 / D} = 0.5 / 1.5 \simeq 0.3$. The hub vortex near wake signature, instead, is defined by $St_{1opt} \simeq \frac{U_c / U_{hub}}{\lambda_1 / D} = 0.5 / 0.7 \simeq 0.7$. While we acknowledge the coarse assumption of the spatial meander traveling with the wake velocity, we also recognize that St_{2opt} is reasonably close to the Strouhal number observed in the turbine far wakes. For example, Medici and Alfredsson¹³ reported values in the range of 0.15 ~ 0.25, Chamorro *et al.*¹⁶ observed a peak at 0.28, while Okulov and Sorensen¹⁸ estimated a peak at 0.23, both at $x/D \simeq 5$. Our estimate of the near wake meandering and $St_{1opt} \simeq 0.7$, instead, is close to values reported by Refs. 35 and 36 in the range of 0.44 ~ 0.81 and recognized as the signature of the hub vortex. As a first approximation, this could be rewritten as a function of the nacelle geometry (of diameter $d \ll D$), leading to $St_{nacelle} = f_s d / U_{hub} \simeq \frac{U_c / U_{hub} d / D}{\lambda_1 / D} \simeq \frac{0.5 \cdot 0.08}{0.7} = 0.06$, still close to the range $0.03 \simeq 0.054$ explored by Ref. 35. These authors however observed that the hub vortex frequency weakly depends on the tip-speed ratio and seems invariant with respect to the rotor angular velocity, suggesting that the root vortex is playing a major role as compared to the sole nacelle. While these mechanisms should be further investigated at utility scale, where the rotor to nacelle ratio is an order of magnitude larger $D/d \simeq O(10^2)$, so far, our results confirm that the hub vortex and the wake meandering obey two different scaling laws, the first one depending on the rotor kinematics, and likely on the blade geometry near the root, and the other depending on the rotor diameter, thus likely on the mere blockage effect exerted by a bluff body. Note that while the hub vortex signature is always present, the large scale wake meandering oscillation tends to be somewhat dampened for turbine operating at optimal regime or within the wake of an upwind turbine. This is obviously reflected by the decrease in the mean wavelength and mean amplitude observed in Figure 7. The weaker signature of large scale wake meander in the optimal tip-speed ratio may also be related to the fact that our field of view is not long enough to capture well the oscillations significantly larger than $2D$. Indeed, if the expansion angle γ decreases, the interaction with the tip vortex structure and the wake shear layer is expected to occur at $x > 2D$, limiting the region where large scale oscillation can be detected. In this sense, the distinction between near and far wake meandering oscillations might be biased and thus regarded as preliminary.

E. Slope and curvature of meandering flows

On the low-pass filtered meander l_f , the normalized slope C_1 and curvature C_2 can be calculated using

$$C_n = \frac{1}{D} \left(\frac{\partial^n l_f(x)}{\partial x^n} \right), \quad (1)$$

where D is the rotor diameter (used for normalization), and n is the order of the derivative (1 or 2) to provide a measure of the slope or curvature of the signal, respectively. The probability density function (pdf) of the computed slope is presented in Figure 9(a). The pdf of the slope for all of the tested configurations can be approximated by a Gaussian distribution; however, a slight shift in the mean is observed (skewed distribution), suggesting an asymmetric wake, as evidenced in the expansion angle statistics. The pdfs in Figure 9(a) can be further separated into two groups. In contrast to the trend observed for γ and λ as a function of the mean wake velocity, the ST Free and ST Opt are shifted together off-center away from the symmetric Gaussian profile while the TT and TT wake cases remain on-center and show slight asymmetry towards the right. The slope C_1 statistically elucidates the directionality of the wake meander. A divergence from a mean slope of zero for the single turbine case shows that there is a primary slope (or direction other than parallel to the x -axis) that occurs for the low speed meander. As the ST Free and ST Opt C_1 distributions collapse, the tip speed ratio appears to have a smaller role on the local slope, as compared to the turbine configuration (ST versus TT). However, the ST Free and ST Optimal cases manifested different wake amplitude A and wavelength λ . These two observations are reconciled if the flow meanders are manipulated, i.e., stretched or compressed, equivalently in both the x and y , wall parallel dimensions, under different TSRs. When one turbine is placed into a more complex configuration, for example the turbine-turbine case, the wake directionality (as defined by the shape of the C_1 pdf) is shifted back toward zero (aligned with the x -axis). Note that this is also seen in the reduction of wake expansion angle γ for the TT case versus ST Free, see Fig. 6(a). Upon interaction of the upwind turbine wake with the second turbine, the new wake formed has a further homogenized scale composition⁴⁴ and thus produces a more symmetric pdf of the wake slope; for reference, a sine wave would produce a slope pdf that is perfectly symmetric about zero. The curvature C_2 , shown in Figure 9(b), is another parameter describing the signature of the low speed meander. The four test cases are split again into two sets (ST Free with TT) and (ST Opt with TT wake), which are the same groupings recognized in the expansion angle, wavelength, and mean wake velocity statistics. This similarity is not a coincidence, as the curvature is very much linked to the strength of the wake edge shear layer and to the opening angle of the wake. In the plot, the ST Free case is the least symmetric followed by the TT, as the front turbine wake is expected to produce more positive wake curvature than negative because of the difference between the left and right wake edge angles. Note that positive curvature is measured at local minima while negative curvature at local maxima. Two

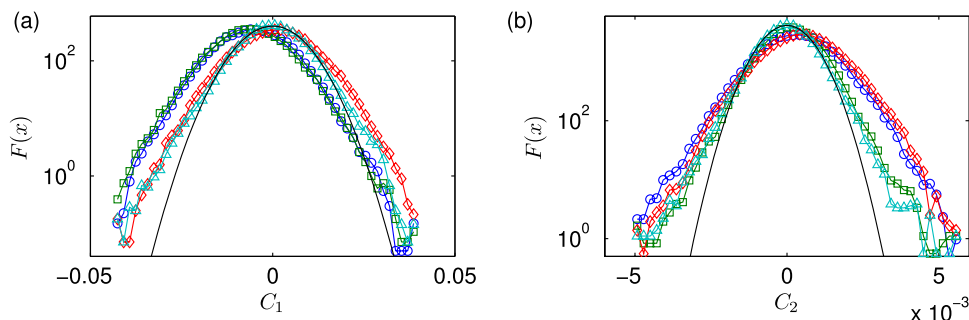


FIG. 9. The low-pass filtered wake is analyzed through the pdfs $F(x)$ normalized such that the area under the curve is equal to unity for (a) the slope and (b) the curvature for each of the turbine tests. The statistics are calculated using all of the instantaneous PIV fields available for each of the runs. \circ represents the single turbine free, \square the single turbine optimal, \diamond the turbine-turbine upwind wake, and \triangle the turbine-turbine downwind wake cases. The solid black curve is a Gaussian distribution with the same mean and standard deviation as the TT wake case.

key features observed in the small range of curvature for the ST Opt and TT wake sets are the near symmetry of the pdfs and the sharp increase in curvature for $C_2 > 4e-3$. The symmetry of the pdfs points out that the meanders for these two cases are closer to a (relatively) low amplitude periodic function, gently increasing in x . It is proposed that the leveling off of curvature near $C_2 \approx 4e-3$ (introduced at higher positive curvature) is the reaction of the wake to the changing intensity of the wake edge shear layer, also reflected in the left-right asymmetry of the wake expansion angle. In summary, the slope and the curvature of the flow meanders are fairly independent features, with the former depending on the rotor directionality, while the latter representing a measure of the stretching and compression of the meander, as described by the amplitude and wavelength.

F. Higher order wake statistics

Utilizing the instantaneous turbine wake PIV fields and the filtered meander signal, we can further analyze wake statistics to understand the mutual interaction between large scale meandering and the small scale vortices generated by sub-shear layers, hub and root vortices, within turbine wake itself. In particular, we focus on the fluctuations ($l' = l_{raw} - l_f$, where l_f is the spatially filtered curve describing the large scale wake meander) and compute their distribution for each of the investigated cases, (Figure 10(a)). The pdfs in the semilog plot suggest a deviation from the Gaussian distribution, with a trend that can be well approximated by a double exponential distribution. The thicker tails are attributed to the increase in the r.m.s of the velocity, to scale interaction mechanisms and intermittency observed in wind turbine wakes and responsible for the complexity of the wake structure.^{15,44,46} A Gaussian pdf with the same mean and standard deviation as the TT wake case is plotted for comparison in Figure 10(a). The four cases here have the same $l'(x)$ pdf profiles over the entire slope range; however, upon closer inspection of the pdf (inset plot showing peak), we find that the TT wake (Δ) has higher peakedness compared to other cases, suggesting slightly weaker tails. It is speculated that the front turbine wake exerts a weak confinement effect, linked to the reduced spanwise expansion of the filtered meandering motion, on the small scale vorticity of the downwind turbine's wake. In other words, we suggest that the different wake meandering characteristics observed in Figures 6 and 7, under different operating regimes, maintain a very weak signature on the small scale turbulence of the wake.

Following the findings of Singh *et al.*⁴⁴ for scale-dependent velocity increments, we define a spatial increment $\Delta l'(x, a) = l'(x + a) - l'(x)$ of the fluctuations $l'(x)$ as a function of the length scale a . Comparison between $a = \Delta x$ (our spatial resolution) and $a = \lambda$ (where λ is the mean wavelength) is shown in Figure 10(b). By indicating with the solid black curve a Gaussian distribution with the same mean and standard deviation for the TT wake case, we note that the tails of the pdf for $a = \lambda$ depart from the Gaussian distribution (hence, thicker tails) but also mildly from the corresponding pdf for $a = \Delta x$. This finding confirms that fluctuations in the meandering wake manifest a multiscale type of behavior, a key physical phenomenon which has been observed in

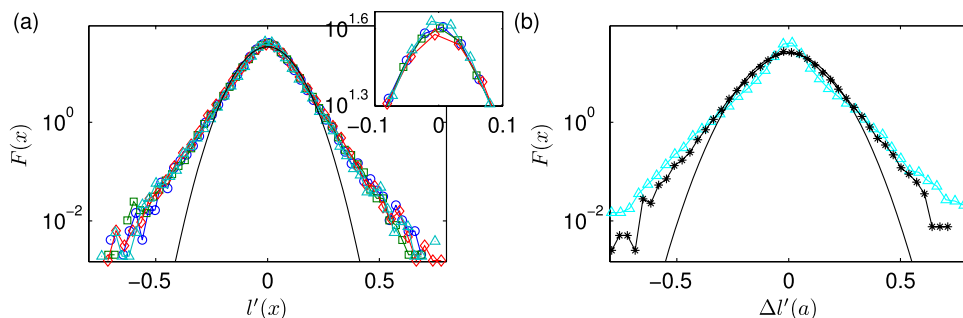


FIG. 10. (a) Semilog plot of the pdfs $F(x)$ of the fluctuations l' for the four cases with the inset showing a zoomed view of the peak; the symbols \circ , \square , \diamond , and Δ represent the single turbine free single turbine optimal, turbine-turbine, and turbine-turbine wake cases, respectively. (b) Pdf of scale-dependent increments $\Delta l'(x, a) = l'(x + a) - l'(x)$ for $a = \Delta x$ (Δ) and $a = \lambda$ ($*$) on the turbine-turbine wake case. The solid black curve is the pdf of a Gaussian distribution with the same mean and standard deviation as the turbine-turbine wake case. All the plots are normalized such that the area under each curve is equal to unity.

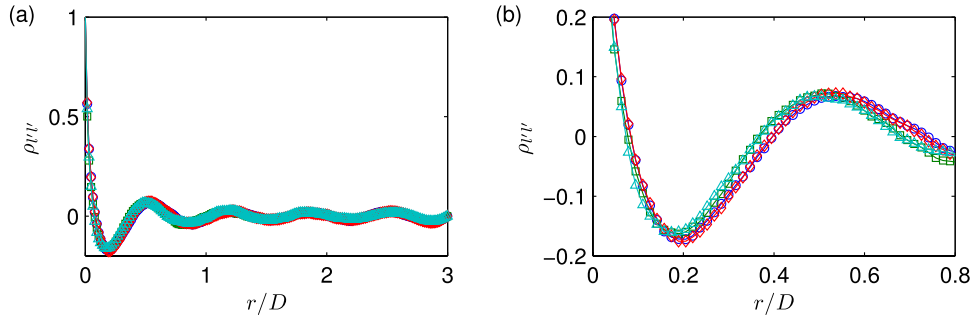


FIG. 11. (a) The auto-correlation of the fluctuations about the filtered wake signals. (b) View of the first and second zero crossings to show the shift in length scales between the different cases. The single turbine free single turbine optimal, turbine-turbine, and turbine-turbine wake cases are shown by symbols \circ , \square , \diamond , and \triangle , respectively.

many natural processes denoting non-local energy transfer and strong scale interactions (Refs. 47 and 48). Both mechanisms were not observed to quantitatively depend on the operating regime and are thus expected to occur in any turbine wake: the key is the large scale meandering, low velocity region, delimited by a likely annular shear layer, interacting with the tip vortices and the surrounding high momentum motions to produce the small scale vortices observed in the instantaneous realization (Figure 4) and referred to, here, as wake fluctuations. Such interactions are further investigated below using the auto-correlation of the streamwise velocity $\rho_{l'l'}(r)$.

In particular, $\rho_{l'l'}(r)$ is calculated to understand if the wake fluctuations have a memory of outside forcing due to their specific location in the wake, or in other words, if the fluctuations manifest some type of structure as they depart from the wake centerline. Here, we define the mean as the trace of the large scale meandering flow patterns l_f , while the fluctuations $l'(x)$ represent the locations of the wake minima departing from the meander due to small vortices generated along the wake. The spatial auto-correlation defined below is semi-Lagrangian in nature, as the meander signature varies in each instantaneous flow field,

$$\rho_{l'l'}(r) = \left\langle \frac{\langle l'(x, n) l'(x + r, n) \rangle_x}{\sigma_{l'(n)}^2} \right\rangle_n, \quad (2)$$

where l' is the $y(x)$ location of the fluctuation about the filtered wake, r is the spatial lag variable, and n marks the instantaneous PIV flow field over which the ensemble average is performed. $\rho_{l'l'}(r)$ is computed for each instantaneous wake $l'(x, n)$ and then ensemble averaged over all runs, producing the four curves presented in Figure 11. It can be seen from Fig. 11(a) that the correlation coefficient reduces from $\rho_{l'l', r=0} = 1$ (as imposed by the normalization) and exhibits, after the first zero crossing, a periodic oscillation for increasing spatial lag r , with the local minima at $r/D \approx 0.2$ (anti-correlation) and a local maxima at $r/D \approx 0.5$ (positive correlation). This correlated/anti-correlated trend continues indefinitely in our domain, thereby producing a smooth, oscillating correlation coefficient. Note that the auto-correlation coefficient of a sine wave produces a perfect correlation at $r = 0$ and is perfectly anti-correlated at $r = \pi$: with this comparison in mind, we infer that the fluctuations about the filtered wake do in fact have a signature (memory) of their location in the wake. The local maxima of the correlation coefficient are roughly spaced at (gradually increasing) $r/D \approx 0.5$, which when referring to Fig. 7(a) is approximately 0.5 of λ for each of the cases. This suggests that the fluctuations occurring near the spanwise extremes (local minima and maxima) about the filtered wake l_f have similar tendencies (and similar forcing from an outside source) for all x locations and are thus driven by their location on the large scale meander developing in the wake. The spatial lag of $0.5 r/D$ is also consistent between the various turbine configurations and highlights the fact that the fluctuations located at the filtered wake minima and maxima exhibit similar trends consistently with the meander curvature. The significance of $0.5r/D$ is that (i) the fluctuations do not specify at which wake extreme ($\pm y$) they are located, but that the outside forcing (wake edge shear layer) produces a statistically similar vortex pair in an alternated pattern with respect to the meander signature; (ii) another estimate of the wavelength could then

be calculated through the auto-correlation of the l' fluctuations. It is proposed that the signature of these outer/inner edge fluctuations is due to the interaction between the wake edge shear layer and the flow meander, resulting in stronger instabilities at maximum curvature locations. It is not clear yet if the low speed meandering oscillations are the cause or the effect of these smaller eddies near the mean wake centerline; it could be speculated that the hub vortex fuels the near wake instability, where smaller eddies are generated, while the latter interacting with the wake shear layer contributes to the wake meander large scale instability. Note that by recognizing the strong spatial periodicity $\lambda = 0.5D$ in the near wake ($x/D < 1$), we can build a Strouhal number $St_{hub} \approx \frac{U_c/U_{hub}}{\lambda/D} = 0.3/0.5 \approx 0.6$ which is well within the hub vortex signature.³⁵ The spatially persistency, though reduced in amplitude, of the periodic autocorrelation suggests that the hub vortex signature persists in the wake up to at least $x = 4D$.

Figure 11(b) shows the zoomed view of $\rho_{l'l'}(r)$ up to the third zero crossing. In this frame, we see that again, two subsets are recognized from the four different test configurations. The two cases with the relatively shorter oscillation period are ST Opt and TT wake, which shows that indeed the large scale meander signature is the defining feature in the auto-correlation function, as these two tests have the shortest wavelengths (Fig. 7(a)). Consistently with the similar incoming boundary conditions, the ST Free and TT curves overlap almost perfectly.

IV. DISCUSSION: ON NEAR AND FAR WAKES

The above results allow us to start a digression on how the far wake instability, known as wake meandering, evolves from near wake features governed by the hub vortex instability and its interactions with tip vortices and the turbine annular shear layer. However, the distinction between the two flow regions is not clear, as the hub vortex signature persists up to $4D$ (at least) while large scale meandering motions may start as early as $2D$. In addition, the low speed meander evolves smoothly displaying wavelengths ranging from $0.5D$ to almost $1.8D$. Given that the hub vortex temporal periodicity seems to be controlled by the rotor kinematics, thus by the root vortex rather than the nacelle shedding, the expansion of the low speed meander within the hub wall normal plane is tip-speed ratio dependent (hence, depending on the turbine operating condition within its performance curve). The fact that the meander rapidly extends to the tip vortex at $y/D = \pm 0.5$ at $x \approx 2D$ introduces a second forcing governed by the wake shear layer which depends on the actual turbine(s) configuration (hence, the wakes of the front turbine rows expand differently as compared to those of the downwind turbines). The reduced mean shear in the turbine-turbine case limits the entrainment of high momentum fluid in the wake, thus the mean wake velocity and the stretching of the meander in the wall parallel plane (reduced wavelength and amplitude). The interaction between the hub vortex and the tip vortices is possibly facilitated by the small scale vorticity generated around the low speed meandering motion and the surrounding shear layer. These structures are likely responsible for the breakup of the tip vortex and the homogenization of turbulence in the wake. As a consequence, (1) the increased r.m.s. of streamwise velocity in the wake is mostly due to an increase of turbulent kinetic energy in the small scales, (2) high-order statistics in the wake are only weakly scale-dependent and weakly depending on the turbine operating conditions. As those moments are computed along the low speed meander, it means that the small scales adjust themselves to the different configurations assumed by the hub vortex. What survives in the far wake is the low speed meandering motion, progressively diffused, and driven now by the wake shear layer, which depends on the velocity deficit and thus on the turbine operating conditions. In summary, the hub vortex is recognized as a key element in the near wake, contributing to the near wake expansion of a meandering low speed region. In the shear layer around this low speed meander, small scale vorticity is formed and starts interacting with the tip vortex. These interactions start as early as $x = 2D$ progressively breaking up the hub and tip vortex structures into a weakly meandering, more homogenized regions of smaller scale turbulence, driven by the wake shear layer (far wake meandering). The resulting large scale oscillations are characterized by a spatial periodicity of about $1.5 - 2D$ as compared to the $0.6 - 0.8D$ characteristic of the hub vortex.

Far wake meandering is thus inferred here to result from a rotor scale, shear type of instability; whether the initiating perturbation is only due to the hub vortex remains however a matter of

debate. In our experiments, we have two key sources of perturbations that contribute to destabilize the tip vortex structure, namely (i) the large scale turbulence of the incoming flow and (ii) the hub vortex. The simulations of Kang, Yang, and Sotiropoulos,³⁴ with an axial turbine placed in a fully developed boundary layer flow, highlighted that different turbine models (actuator disk, lines, fully resolved geometry) with identical inflow conditions all lead to a meandering wake, though with different intensities and extensions of the near wake regions. Kang *et al.* showed that the Large Eddy Simulation (LES) resolving the geometrical details of the turbine, and thus accounting for the effect of geometry-induced pressure gradients on the flow in the immediate vicinity of the nacelle, yielded a hub vortex that undergoes a spiral mode instability immediately downstream of the nacelle giving rise to a very energetic meandering zone that gradually spreads radially and ultimately begins to interact with the turbine tip shear layer. This interaction dramatically augments the intensity and spatial extent of the outer wake meandering zone. Actuator based models either do not predict a hub vortex at all (non-rotating actuator disk) or predict a hub vortex that remains stable and columnar confined along the turbine axis (rotating actuator lines). In both cases, the far-wake meandering region is less energetic and shorter than that arising in the turbine geometry resolving LES. This suggests that when the incoming flow is a fully developed turbulent boundary layer, the large-scale instability of the hub vortex, while it is not the necessary condition for far-wake meandering to be triggered, it can augment the intensity and spatial extent of the flow meanders. The work of Kang *et al.*, however, did not investigate the linkages between hub vortex instability and wake meandering as a function of incoming turbulence intensity or mean shear, including the limiting case of steady and vertically homogeneous incoming flow. We are thus still not able to quantify the separate effects of ambient wall turbulence and hub vortex on the amplitude and intensity of wake meandering, especially in relevant turbine configurations such as the fully developed wind power plant that was not investigated here. Regarding the potential role of the nacelle size, we stress that the nacelle to rotor diameter ratio in our turbine model is approximately half of the corresponding value for the hydrokinetic instream turbine simulated by Kang, Yang, and Sotiropoulos:³⁴ the consistency of the current experimental results with the simulation suggests that the hub vortex effect on the wake is robust, and reasonably independent from the actual nacelle size.

V. SUMMARY AND CONCLUSIONS

Two dimensional velocity measurements collected up to $4D$ downwind of a model wind turbine via a spatially resolved wall-parallel PIV setup were analyzed to quantitatively describe wake meandering under four different turbine operating conditions and configurations. The turbine wake meander signature was first identified as the low-pass filtered signal of the minimum streamwise velocity at each x -location. The spatial filter was introduced to distinguish between the smooth meandering pattern, resembling those observed by geomorphology community in rivers and streams, from smaller eddies formed around the center of the meander and statistically representing spatial fluctuations. Wake statistics, including the mean expansion angle, meander wavelength, and mean wake velocity, along with higher order statistics relating the meandering signature (slope, curvature) with the nearby eddies (auto-correlation function) allowed us to highlight the following results.

- The wake mean expansion angle γ , measured from the centerline axis of the turbine to the left ($+y$) and right ($-y$) wake edges, (i) is not symmetric about the centerline due to the fixed rotation direction of the turbine rotor, (ii) was observed to vary between 4.1° and 6.2° , and (iii) was found to depend on the turbine operation regime within its performance curve (at optimal TSR, a relatively lower γ) and thus on the mean velocity deficit and subsequent shear layer intensity.
- A large scale wake meander was identified through the low-pass filtered signal of the streamwise velocity minima at each x -location downwind of the turbine. The oscillating curve was described in terms of wavelength and local slope and curvature distributions. The mean wavelength of the wake meander λ , varying from $0.8D$ to $1.2D$ between the four configurations tested, was found to be correlated with the mean wake velocity U_c in the wake, suggesting a weak compressing or stretching mechanism driven by the turbine operating regime and velocity deficit. In particular, similarity in the slope pdfs between the ST Free and ST Opt

cases confirms that compression/stretching of the wake meander occurs in both streamwise and spanwise directions, consequently reducing/increasing the meander amplitude and wavelength. At peak performance, the velocity deficit is minimum, the meander is compressed in amplitude, wavelength, and expansion angle, implying that its interaction with the wake shear layers occurs farther from the rotor (as compared to the higher rotational velocity ST free operational regime). In the aligned turbine case, the wake of the downwind turbine experiences a confinement effect resulting in a weaker meandering motion limited by the reduced velocity gradient between outer and wake flows.

- By further inspecting the distribution of meander wavelength and amplitude, two different populations characterized by $\lambda \approx 0.7D$ and $\lambda \approx 1.5D$ were distinguished and related to the hub vortex signature near the wake $x < 2D$ and to a larger scale oscillation in the far wake (wake meandering). The reconstructed Strouhal number for each oscillation type was found to be consistent with literature results in the far wake^{13,16,18} and in the near wake,^{35,36} respectively.
- The low speed meander signature evolving along the full domain up to $x = 4D$ investigated here is inferred to spatially evolve by interacting with smaller scale eddies likely generated in the shear region between the hub vortex and the tip vortices. Those eddies are treated statistically as spatial fluctuations of the wake meander and produce a non-Gaussian distribution of the local slope and a weakly scale dependent distribution of the slope increments. This finding suggests a marked multiscaling behavior governed by non-local (scale) interactions and energy transfer. Physically, this means that the small eddies are intrinsically coupled with the spatial evolution of the low speed meander.
- The auto-correlation of the fluctuations about the low speed meander shows fairly persistent spatial periodicity of $\approx 0.5D$ (along the meander), regardless of the turbine conditions. This suggests that the hub vortex maintains a persistent, though weak, signature in the wake, with small scale vorticity adjusting to (or governing) its wavelength and amplitude. It is proposed that the velocity fluctuations which occur near the meander local minima and maxima experience higher shear, as compared to those near the center of the wake: this mechanism is able to sustain the observed vortices and the meandering flows, especially when the latter comes in contact with the tip vortices and the wake shear layer.

The findings presented above not only provide validation data for turbine wake models but also detailed information on wake oscillations that can be useful for prediction of downwind turbine performance and structural loading, as well as for improving coordinated controllers in multi-turbine arrays. We acknowledge however that wake meandering data have been obtained only up to a distance of $4D$ from the rotor plane, implying that the extrapolation of these results to the far wake at high spatial resolution is not straightforward. Also, even though this turbine model was observed to correctly reproduce the upwind blockage effect and velocity deficit of a utility-scale turbine (between $1.5D < x < 3D$),⁴⁹ it is not obvious that the wake meander and higher order statistics shown here can be used for full-scale units with a rotor Reynolds number $Re = U_{hub}D/\nu \approx 800$ times larger. In addition, while the effect of large scale atmospheric turbulence is accounted for, the investigated turbine configurations do not include the fully developed wind farm, where the DWM model²⁶ is often applied, implying that the generalization of current results to fully developed wind power plants has to be taken with caution. In particular, the characteristic wavelength and amplitude of wake meandering oscillations might be different, even though the scaling with the rotor diameter is inferred to hold. Our work suggests that the definition of near and far wake is weakly depending on the turbine operational conditions, as the meandering motions initiated by the hub vortex are more or less stretched along the wall normal hub plane and thus likely to interact with the tip vortex and the wake shear layer at a different distance from the rotor. While this interaction is observed to start at around $x = 2D$, a weak signature of the hub vortex is shown to persist up to $x = 4D$, due to the small scale vortices paired along the low speed meander. As a result of this, the transition between a near wake region dominated by the rotor kinematics and a far wake region driven by the wake shear layer is smooth and modulated through the low speed meandering motion's amplitude, velocity, and wavelength.

ACKNOWLEDGMENTS

The study presented herein has been supported by the Institute on Environment (IREE funding) at the University of Minnesota, and by the NSF Career (M. Guala). Special thanks goes to Professor Peter Seiler and Jennifer Annoni for the insight into turbine wake models and the help in the experimental characterization of the turbine operational regimes.

- ¹ L. B. Leopold and W. B. Langbein, "River meanders," *Sci. Am.* **214**(6), 60-70 (1996).
- ² A. D. Howard and A. T. Hemberger, "Multivariate characterization of meandering," *Geomorphology* **4**, 161-186 (1991).
- ³ G. Seminara, "Fluvial sedimentary patterns," *Annu. Rev. Fluid Mech.* **42**, 43-66 (2010).
- ⁴ J. Peakall, B. McCaffrey, and B. Kneller, "A process model for the evolution, morphology, and architecture of sinuous submarine channels," *J. Sediment. Res.* **70**(3), 434-448 (2000).
- ⁵ G. Seminara, "Meanders," *J. Fluid Mech.* **554**, 271-297 (2006).
- ⁶ J. W. Lauer and G. Parker, "Net local removal of floodplain sediment by river meander migration," *Geomorphology* **96**(1-2), 123-149 (2008).
- ⁷ E. Meiburg and B. Kneller, "Turbidity currents and their deposits," *Annu. Rev. Fluid Mech.* **42**, 135-156 (2010).
- ⁸ P. A. Nelson and G. Seminara, "A theoretical framework for the morphodynamics of bedrock channels," *Geophys. Res. Lett.* **39**, L06408, doi:10.1029/2011GL050806 (2012).
- ⁹ T. M. Dracos, M. Giger, and G. H. Jirka, "Plane turbulent jets in a bounded fluid layer," *J. Fluid Mech.* **241**, 587-614 (1992).
- ¹⁰ J. C. Rowland, M. T. Stacey, and W. E. Dietrich, "Turbulent characteristics of a shallow wall-bounded plane jet: Experimental implications for river mouth hydrodynamics," *J. Fluid Mech.* **627**(1), 423-449 (2009).
- ¹¹ J. R. Landel, C. P. Caulfield, and A. W. Woods, "Meandering due to large eddies and the statistically self-similarity of quasi-two-dimensional jets," *J. Fluid Mech.* **692**, 247-268 (2012).
- ¹² G. Mariotti, F. Falcini, N. Geleynse, M. Guala, and S. Fagherazzi, "Why meandering turbulent jets have high sediment eddy diffusivity: Implications for levees formation," *J. Geophys. Res.* **118**(3), 1908-1920, doi:10.1002/jgrf.20134 (2013).
- ¹³ D. Medici and P. H. Alfredsson, "Measurements behind model wind turbines: Further evidence of wake meandering," *Wind Energy* **11**(2), 211-217 (2008).
- ¹⁴ G. Espana, S. Aubrun, S. Loyer *et al.*, "Spatial study of the wake meandering using modelled wind turbines in a wind tunnel," *Wind Energy* **14**(7), 923-937 (2011).
- ¹⁵ J. Hong, M. Toloui, L. P. Chamorro, M. Guala, K. B. Howard, S. Riley, J. Tucker, and F. Sotiropoulos, "Natural snowfall reveals large-scale flow structures in the wake of a 2.5-MW wind turbine," *Nat. Commun.* **5**, 4216 (2014).
- ¹⁶ L. P. Chamorro, C. Hill, S. Morton *et al.*, "On the interaction between a turbulent open channel flow and an axial-flow turbine," *J. Fluid Mech.* **716**, 658-670 (2013).
- ¹⁷ V. L. Okulov and J. N. Sørensen, "Stability of helical tip vortices in a rotor far wake," *J. Fluid Mech.* **576**, 125 (2007).
- ¹⁸ V. L. Okulov, I. V. Naumov, R. F. Mikkelsen, I. K. Kabardin, and J. N. Sørensen, "A regular Strouhal number for large-scale instability in the far wake of a rotor," *J. Fluid Mech.* **747**, 369-380 (2014).
- ¹⁹ L. J. Vermeer, J. N. Sørensen, and A. Crespo, "Wind turbine wake aerodynamics," *Prog. Aerosp. Sci.* **29**(6-7), 467-510 (2003).
- ²⁰ J. F. Ainslie, "Calculating the flowfield in the wake of wind turbines," *J. Wind Eng. Ind. Aerodyn.* **27**(1), 213224 (1988).
- ²¹ M. Bastankhah and F. Porté-Agel, "A new analytical model for wind-turbine wakes," *Renewable Energy* **70**, 116-123 (2014).
- ²² R. L. Panton, *Incompressible Flow* (John Wiley & Sons, Inc., Hoboken, New Jersey, 2005).
- ²³ S. Frandsen, R. Barthelmie, R. Pryor, O. Rathmann, S. Larsen, J. Hojstrup, and M. Thøgersen, "Analytical modelling of wind speed deficit in large offshore wind farms," *Wind Energy* **9**, 3953 (2006).
- ²⁴ X. Yang, K. B. Howard, M. Guala, and F. Sotiropoulos, "Effects of a three-dimensional hill on the wake characteristics of a model wind turbine," *Phys. Fluids* **27**, 025103 (2015).
- ²⁵ R. J. Barthelmiw, L. Folkerts, G. C. Larsen, K. Rados, S. C. Pryor, S. T. Frandsen, B. Lange, and G. Schepers, "Comparison of wake model simulations with offshore wind turbine wake profiles measured by sodar," *J. Atmos. Oceanic Technol.* **23**(7), 888-901 (2006).
- ²⁶ G. C. Larsen, H. A. Madsen, K. Thomsen, and T. J. Larsen, "Wake meandering: A pragmatic approach," *Wind Energy* **11**, 377-395 (2008).
- ²⁷ R. E. Keck, M. de Maré, M. J. Churchfield, S. Lee, G. C. Larsen, and H. A. Madsen, "On atmospheric stability in the dynamic wake meandering model," *Wind Energy* **17**(11), 1689-1710 (2014).
- ²⁸ M. S. Adaramola and P. A. Krogstad, "Experimental investigation of wake effects on wind turbine performance," *Renewable Energy* **36**, 2078-2086 (2011).
- ²⁹ J. Whale, K. H. Papadopoulos, C. G. Anderson, C. G. Helmis, and D. J. Skyner, "A study of the near wake structure of a wind turbine comparing measurements from laboratory and full-scale experiments," *Sol. Energy* **56**(6), 621-633 (1996).
- ³⁰ J. Whale, C. G. Anderson, C. G. Bareiss, and R. Wagner, "An experimental and numerical study of the vortex structure in the wake of a wind turbine," *J. Wind Eng. Ind. Aerodyn.* **84**, 1-21 (2000).
- ³¹ D. Medici and A. Alfredsson, "Measurements on a wind turbine wake: 3D effects and bluff body vortex shedding," *Wind Energy* **9**, 219-236 (2006).
- ³² P. Chatelain, S. Backaert, G. Winckelmans, and S. Kern, "Large eddy simulation of wind turbine wakes," *Flow, Turbul. Combust.* **91**, 587-605 (2013).
- ³³ M. L. Aitken, R. M. Banta, Y. L. Pichugina, and J. K. Lundquist, "Quantifying wind turbine wake characteristics from scanning remote sensor data," *J. Atmos. Oceanic Technol.* **31**(4), 765787 (2014).
- ³⁴ S. Kang, X. Yang, and F. Sotiropoulos, "On the onset of wake meandering for an axial flow turbine in a turbulent open channel flow," *J. Fluid Mech.* **744**, 376-403 (2014).
- ³⁵ F. Viola, G. V. Iungo, S. Camarri, F. Porté-Agel, and F. Gallaure, "Prediction of the hub vortex instability in a wind turbine wake: Stability analysis with eddy-viscosity models calibrated on wind tunnel data," *J. Fluid Mech.* **750**, R1 (2014).

- ³⁶ G. V. Iungo, F. Viola, S. Camarri, F. Porte-Agel, and F. Gallaire, "Linear stability analysis of wind turbine wakes performed on wind tunnel measurements," *J. Fluid Mech.* **737**, 499-526 (2014).
- ³⁷ R. B. Cal, J. Lebron, L. Castillo, H. S. Kang, and C. Meneveau, "Experimental study of the horizontally averaged flow structure in a model wind-turbine array boundary layer," *J. Renewable Sustainable Energy* **2**, 013106 (2010).
- ³⁸ N. Hutchins and I. Marusic, "Evidence of very long meandering features in the logarithmic region of turbulent boundary layers," *J. Fluid Mech.* **579**, 1-28 (2007).
- ³⁹ M. Guala, M. Metzger, and B. J. McKeon, "Interactions within the turbulent boundary layer at high Reynolds number," *J. Fluid Mech.* **666**, 573-604 (2011).
- ⁴⁰ L. P. Chamorro and F. Porté-Age, "A wind-tunnel investigation of wind-turbine wakes: Boundary-layer turbulence effects," *Boundary-Layer Meteorol.* **132**, 129-149 (2009).
- ⁴¹ G. España, S. Aubrun, S. Loyer, and P. Devinant, "Wind tunnel study of the wake meandering downstream of a modelled wind turbine as an effect of large scale turbulent eddies," *J. Wind Eng. Ind. Aerodyn.* **101**, 24-33 (2012).
- ⁴² H. Hu, Z. Yang, and P. Sarkar, "Dynamic wind loads and wake characteristics of a wind turbine model in an atmospheric boundary layer wind," *Exp. Fluids* **52**, 1277-1294 (2012).
- ⁴³ K. B. Howard, J. S. Hu, L. P. Chamorro, and M. Guala, "Characterizing the response of a wind turbine model under complex inflow conditions," *Wind Energy* **18**(4), 729-743 (2015).
- ⁴⁴ A. Singh, K. B. Howard, and M. Guala, "On the homogenization of turbulent flow structures in the wake of a model wind turbine," *Phys. Fluids* **26**, 025103 (2014).
- ⁴⁵ R. J. Adrian, K. T. Christensen, and Z. C. Liu, "Analysis and interpretation of instantaneous turbulent velocity fields," *Exp. Fluids* **29**(3), 275-290 (2000).
- ⁴⁶ L. P. Chamorro, M. Guala, R. E. A. Arndt, and F. Sotiropoulos, "On the evolution of turbulent scales in the wake of a wind turbine model," *J. Turbul.* **13**, 1-13 (2012).
- ⁴⁷ Y. Malecot, C. Auriault, H. Kahalerras, Y. Gagne, O. Chanal, B. Chabaud, and B. Castaing, "A statistical estimator of turbulence intermittency in physical and numerical experiments," *Eur. Phys. J. B* **16**, 549561 (2000).
- ⁴⁸ A. Singh, E. Foufoula-Georgiou, F. Porté-Agel, and P. R. Wilcock, "Coupled dynamics of the co-evolution of gravel bed topography, flow turbulence and sediment transport in an experimental channel," *J. Geophys. Res.* **117**, F04016, doi:10.1029/2011JF002323 (2012).
- ⁴⁹ K. B. Howard, Ph.D. thesis, University of Minnesota, 2014.